On the Thermal Performance of a Microparallel Channels Heat Exchanger

Ivana Fernandes de Sousa
Laboratory of Nano and Microfluidics and Micro-Systems—LabMEMS,
Engineering of Nanotechnology Department,
Federal University of Rio de Janeiro—UFRJ,
Rio de Janeiro 21.941-594, Brazil

Carolina Palma Naveira Cotta[1]
Laboratory of Nano and Microfluidics and Micro-Systems—LabMEMS,
Mechanical Engineering Department,
Federal University of Rio de Janeiro—UFRJ,
Rio de Janeiro 21.941-594, Brazil;
Nanoengineered Systems Laboratory,
UCL Mechanical Engineering,
University College London,
London WC1E 6BT, UK
e-mail: carolina@mecanica.coppe.ufrj.br

Daduí Cordeiro Guerrieri
Mechanical Engineering Department,
CEFET-RJ UnED Itaguaí,
Rio de Janeiro 23.812-101, Brazil

Manish K. Tiwari
Nanoengineered Systems Laboratory,
UCL Mechanical Engineering,
University College London,
London WC1E 7HB, UK

This paper presents the experimental and theoretical analysis of a micro heat exchanger designed for the waste heat recovery from a high concentration photovoltaic (HCPV) system. A test bench was built to analyze the thermal behavior of a heat exchanger targeted to work in a similar condition of an existing HCPV panel. A high power heater was encapsulated inside a copper cartridge, covered by thermal insulation, leading to dissipated heat fluxes around 0.6 MW/m^2, representative of the heat flux over the solar cell within the HCPV module. The experimental campaign employed water as the coolant fluid and was performed for three different mass flow rates. An infrared camera was used to nonintrusively measure the temperature field over the micro heat exchanger external surface, while thermocouples were placed at the contact between the heat exchanger and the heater, and at the water inlet and outlet ports. In the theoretical analysis, a hybrid numerical–analytical treatment is implemented, combining the numerical simulation through the COMSOL MULTIPHYSICS finite elements code for the micro heat exchanger, and the analytical solution of a lumped-differential formulation for the electrical heater cartridge, offering a substantial computational cost reduction. Such computational simulations of the three-dimensional conjugated heat transfer problem were critically compared to the experimental results and also permitted to inspect the adequacy of a theoretical correlation based on a simplified prescribed heat flux model without conjugation effects. It has been concluded that the conjugated heat transfer problem modeling should be adopted in future design and optimization tasks. The analysis demonstrates the enhanced heat transfer achieved by the microthermal system and confirms the potential in reusing the recovered heat from HCPV systems in a secondary process.
[DOI: 10.1115/1.4041439]

Keywords: micro heat exchanger, microchannels, conjugated heat transfer, HCPV system, waste heat recovery, infrared thermography

1 Introduction

According to the United Nations, global energy and food demand are predicted to increase by around 50% by 2030, while that of water by 30% [1,2]. The depleting earth resources and increasing demand due to projected rise in global population and urbanization make it imperative to develop novel sustainable technologies. For instance, integrating water-cooled high concentration photovoltaic (HCPV) systems with one or more waste heat recovery technologies can have major positive impact on water, energy, food, healthcare and environmental challenges, being well-aligned with the idea of sustainable development. HCPV systems exploit concentrated solar flux using cheap optical components in lieu of large area and expensive photovoltaic cells. However, HCPV chips—due to their higher energy flux—generate considerable amount of heat which not only lowers their energy conversion efficiency drastically but also gets wasted. Novel microscale water cooling systems [3–8] can effectively regulate the photovoltaics cell temperature, thereby enhancing the cell energy efficiency [9–15]. The heat extracted by the coolant can, for instance, be reused in food and pharmaceutical storage, through an absorption cycle microrefrigeration unit, such as for food preservation and storage of vaccines, in membrane-based water desalination processes to make saline water suitable for human and agricultural use, and in the efficient continuous synthesis of biodiesel [15–20].

Concerning the conception and design of microheat exchangers, numerous works are still aimed at the investigation of the most adequate models and solution methodologies for describing the physical phenomena that take place in such microscale heat transfer devices. For instance, it has been observed for different microscale applications that effects such as conjugated conduction–convection, axial fluid heat conduction, viscous dissipation, rarefaction and compressibility, can be essential in appropriately predicting heat transfer rates. Correlations for oversimplified theoretical formulations and/or experimental correlations from data originally obtained for macroscale problems, when such effects are indeed irrelevant, may lead to erroneous predictions for thermal microdevices [21–26].

In this context, the experimental part of this study is aimed at obtaining accurate temperature measurements using both thermocouples and infrared thermography, so as to assess the influence of conjugate heat transfer effects in such microthermal systems, for different values of the coolant mass flow rate. The experimental temperature results are then critically compared with the numerical predictions. The theoretical analysis introduces a relevant improvement in terms of computational cost reduction, by combining analytical and numerical solution procedures. The temperature field in the electric heater cartridge is handled analytically, by implementing a lumped-differential formulation for the two-dimensional transient heat conduction problem, through the so-called coupled integral equations approach (CIEA) [27–31]. The solution for the micro heat exchanger is then obtained

[1]Corresponding author.

Contributed by the Heat Transfer Division of ASME for publication in the JOURNAL OF THERMAL SCIENCE AND ENGINEERING APPLICATIONS. Manuscript received May 23, 2018; final manuscript received September 3, 2018; published online October 31, 2018. Assoc. Editor: Pedro Mago.

through the finite element method, implemented in the commercial COMSOL MULTIPHYSICS platform [32], solving for the associated conjugated heat transfer model with adequate boundary conditions suited to the experiments. In addition, the numerical results from this three-dimensional conjugated heat transfer model are employed to inspect for the adequacy of a theoretical correlation for simplified prescribed wall heat flux condition, in estimating the corresponding global heat transfer coefficient for the analyzed microthermal device, aimed at its adoption in future optimization and design tasks.

2 Experimental Work

2.1 Micro Heat Exchanger. Correa et al. [2] designed a micro heat exchanger for active cooling of a commercial HCPV module that concentrates 1200 suns (Sunflower, ATS Pyron), using water as working fluid in a closed loop. This device was fabricated by micromilling, and a subsequent numerical and experimental analysis was carried out by Guerrieri and Naveira-Cotta [1].

However, the geometries of the inlet and outlet exchanger plenums were not optimized by Correa et al. [2] and Guerrieri et al. [1], who proposed just a plain rectangular plenum for the fluid distribution and collection. Nevertheless, it is well known that a rectangular plenum favors a flow maldistribution [33–35]. In fact, the simulation of the flow distribution for the micro heat exchanger studied by Correa et al. [2] and Guerrieri et al. [1], employing the COMSOL MULTIPHYSICS software [32], confirms such a maldistribution of fluid flow among the microchannels, as one can see by the simulated fully developed velocity profile, provided in Ref. [1], for each microchannel in Fig. 1.

This work was then first aimed at implementing such an improvement in the design of the originally proposed micro heat exchanger [1,2]. The present microdevice has a total of 24 microchannels and was built with a trapezoidal geometry for the inlet and outlet plenums, so as to minimize the maldistribution of the fluid flow among the microchannels. Figure 2 presents the technical drawing and detailed dimensions for the base and cover of the redesigned micro heat exchanger. Then, Fig. 3 presents the COMSOL simulated velocity profiles for the same input conditions adopted by Guerrieri and Naveira-Cotta [1] and presented in Fig. 1, but considering this new heat exchanger configuration with trapezoidal plenums, which results in a more uniform fluid flow distribution within the channels when compared to the previous rectangular plenums configuration proposed in Refs. [1] and [2] (Fig. 1). It was observed as a reduction on the standard deviation of the averaged maximum velocity from 12.8% for rectangular plenums to a 5.4% standard deviation for the trapezoidal plenums. The inclination for this trapezoidal plenum was determined through a parametric analysis in the fluid flow numerical simulation within the micro heat exchanger varying from 0 deg (rectangular plenum) to 25 deg (trapezoidal plenum), achieving the minimum standard deviation of 5.4% in the averaged maximum velocity at an angle of 10 deg.

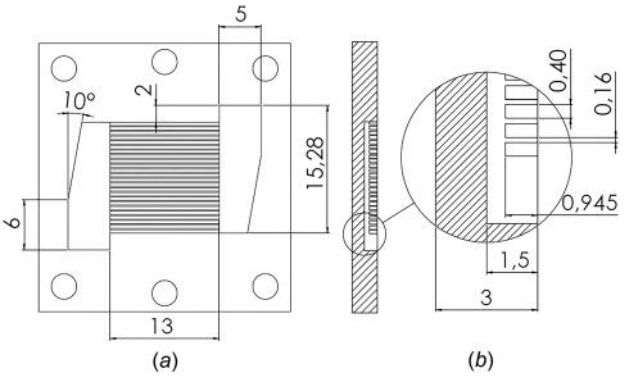

Fig. 2 Technical drawings of the proposed micro heat exchanger: (*a*) open view of the bottom plate and (*b*) channel details and dimensions

The micro heat exchanger here analyzed was then manufactured in aluminum with a micromilling CNC machine from Minitech Machinery Corporation, containing 24 microchannels with a cross section of 400 μm × 945 μm and 13 mm in length, and milling tolerance of 1 μm (see Fig. 2). The final surface area occupied only by the microchannels, of 172.64 mm^2, as highlighted in Fig. 2, was designed to be the same as the area of the commercial solar cell manufactured by Azur Space Solar Power GMBH (type 3C42A), as presented in a closer view in Fig. 4. The overall dimensions of the sealed device are: 21.05 mm in width, 35.02 mm in length, and 0.82 mm in thickness. The fabricated micro heat exchanger is presented in Fig. 5(*a*), in an open view. Additionally, for sealing purposes, four screws were fixed at the corner of the micro heat exchanger and two extras, on both sides, were used to fix the heat exchanger in the main solar board, also depicted in Fig. 5(*b*).

2.2 Test Setup. In the experimental setup, distilled water was employed as the cooling fluid, which is withdrawn from the reservoir and pumped into the system (the micro heat sink mounted solar cell) using a helicoidal positive displacement pump controlled by a frequency inverter and able to steadily operate at low mass flow rates (Netzsch, NM003BY11S12B). At the outlet of the micro heat exchanger, the fluid is stored in the container placed over an electronic scale to measure the mass flow rate.

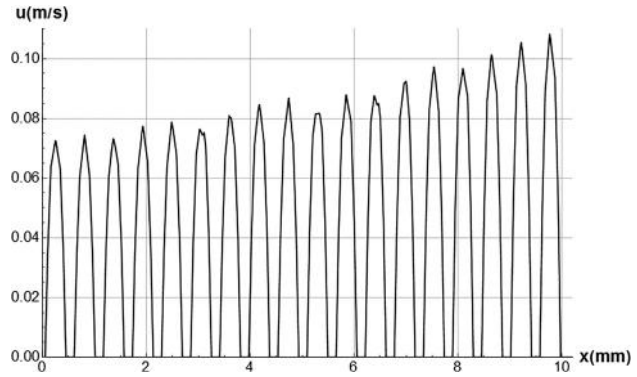

Fig. 1 COMSOL simulated velocity profile for each microchannel with a rectangular plenum, Guerrieri et al. [1]

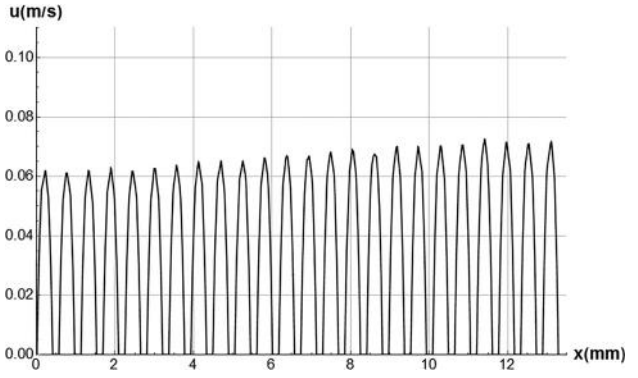

Fig. 3 COMSOL simulated velocity profile for each microchannel for the proposed micro heat exchanger with trapezoidal plenums

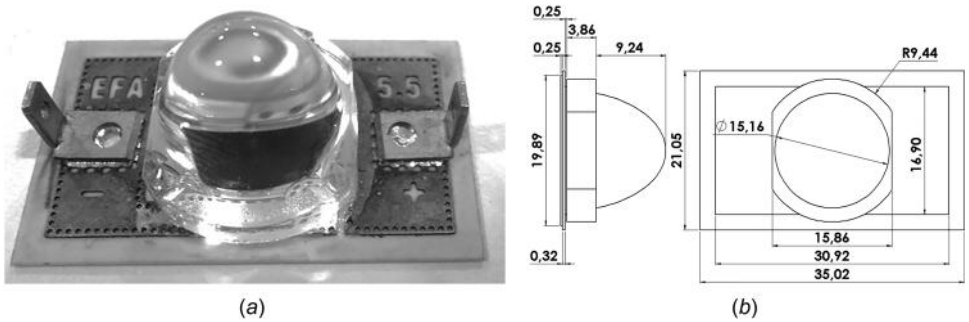

Fig. 4 Azur space solar cell (type 3C42A): (*a*) actual picture and (*b*) schematic drawing

The heater used in the apparatus was selected considering a desired direct normal solar energy incidence of 600 W/m^2 that, according to Correa et al. [2], is a representative average value from the Rio de Janeiro region. Then, combining this direct normal solar energy with a Fresnel Lens with capacity of concentration of 1000 times (Knight Optical), the incident irradiation over the cell would be around 0.6 MW/m^2. To achieve this power level within the experimental setup, an electrical heater of 238 Ω was chosen, which had a maximum dissipated power of 67.76 W at 127 V (AC). The dimensions of the heater are: 8.0 mm of radius, 60 mm in length positioned inside a specially prepared copper cartridge to direct a uniform heat flow to an area of 10×10 mm^2, where the micro heat exchanger is positioned, and thus limited to a theoretical maximum heat flux of 0.67 MW/m^2. Figure 6 depicts the electrical heater inside the copper cartridge with the related dimensions. To minimize heat losses, the whole heating module was covered with thermal insulation made of fiberglass (Termovid 901) with 3.25 cm of thickness in the radial direction. Table 1 presents the dimensions of the copper cartridge and of the thermal insulation around the cartridge. The insulation under the cartridge is square shaped with a dimension of 75.7 mm × 75.7 mm and 3 mm of thickness.

Figure 7 illustrates the experimental hydraulic circuit, and Fig. 8 shows the overall experimental setup, comprising the following devices: an acquisition data system Agilent 34972-A (*a*), a computer for data acquisition (*b*), a calibrated infrared thermographic camera (Flir SC645) (*c*), the heat exchanger, the heater system, and insulation (*d*), and the electronic scale (*e*).

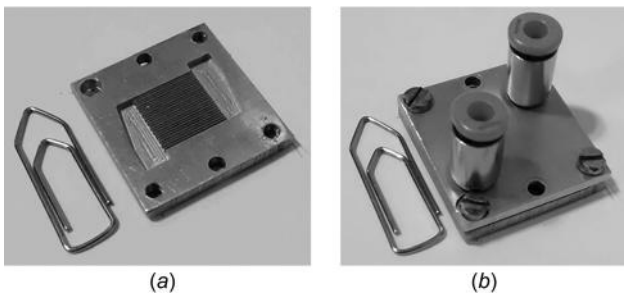

Fig. 5 Fabricated micro heat exchanger: (*a*) open view of the heat exchanger bottom plate and (*b*) closed view of the heat exchanger

Table 1 Dimensions of the thermal insulation

Parameter (Unit)	Value
r_i (m)	7.5×10^{-3}
r_e (m)	4×10^{-2}
H (m)	7.4×10^{-2}

The transient temperature measurements were performed using the infrared camera to capture the temperature distribution on the top external surface of the exchanger. Also, five thermocouples were placed at different essential locations: at the inlet (tp1) and outlet (tp2) fluid connections, at the contact of the heating system and the micro heat exchanger (tp3), at the lateral external surface of the heating system insulation (tp4), as schematically shown in Fig. 9, and a last one (tp5) measuring the ambient temperature (not shown in the figure). In Fig. 9, it can also be seen that the top surface of the micro heat exchanger is painted with a graphite ink to a known value of emissivity (0.97), reported by the paint

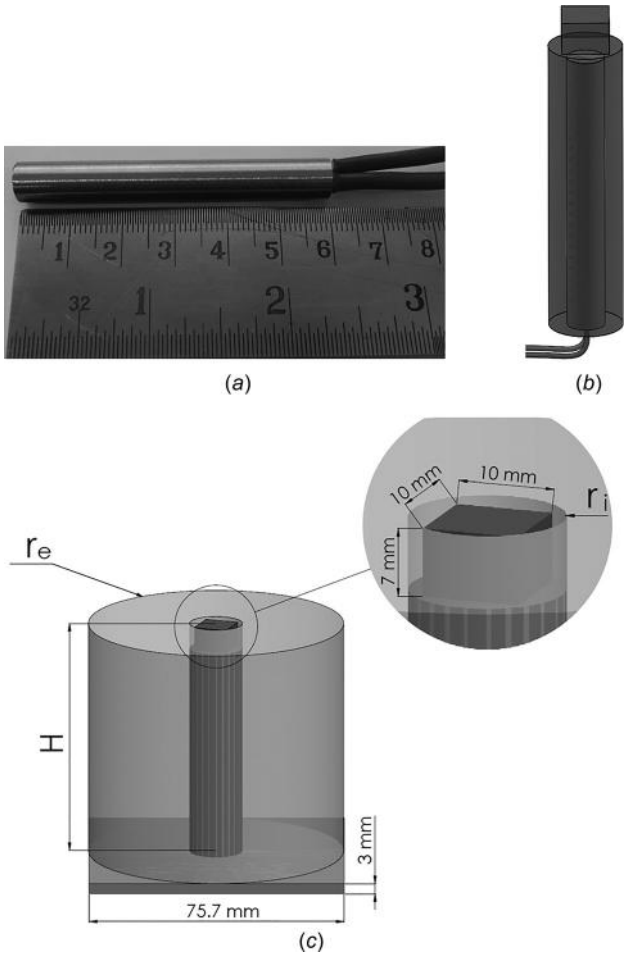

Fig. 6 Schematic drawing of the heating system assembly with the external insulation cover: (*a*) electrical cylindrical heater, (*b*) schematic drawing of the heater inside the copper cartridge, and (*c*) dimensions of the copper cartridge and thermal insulation

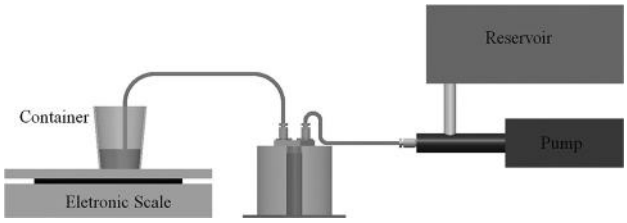

Fig. 7 Schematic drawing of the hydraulic circuit

manufacturer (Graphit 33, Kontact Chemie), for accurate thermographic measurements.

2.3 Test Procedure. The experiments were started with the pump set to a constant water mass flow rate of 20, 24, or 28 g/min, with the uncertainties in the flow rate being $\pm 1\%$ of the measured value. The temperature measurement devices are then started, still without heating. Then, the electrical heater is turned on. All the measurements are monitored with the Agilent (34972-A) data acquisition system connected to a computer. Along the experiment duration, the temperatures at the external surface of the micro heat exchanger are recorded with the infrared camera (FLIR SC645). Temperature measurements were continuously collected at 10 s intervals. Steady-state is reached within 60 min

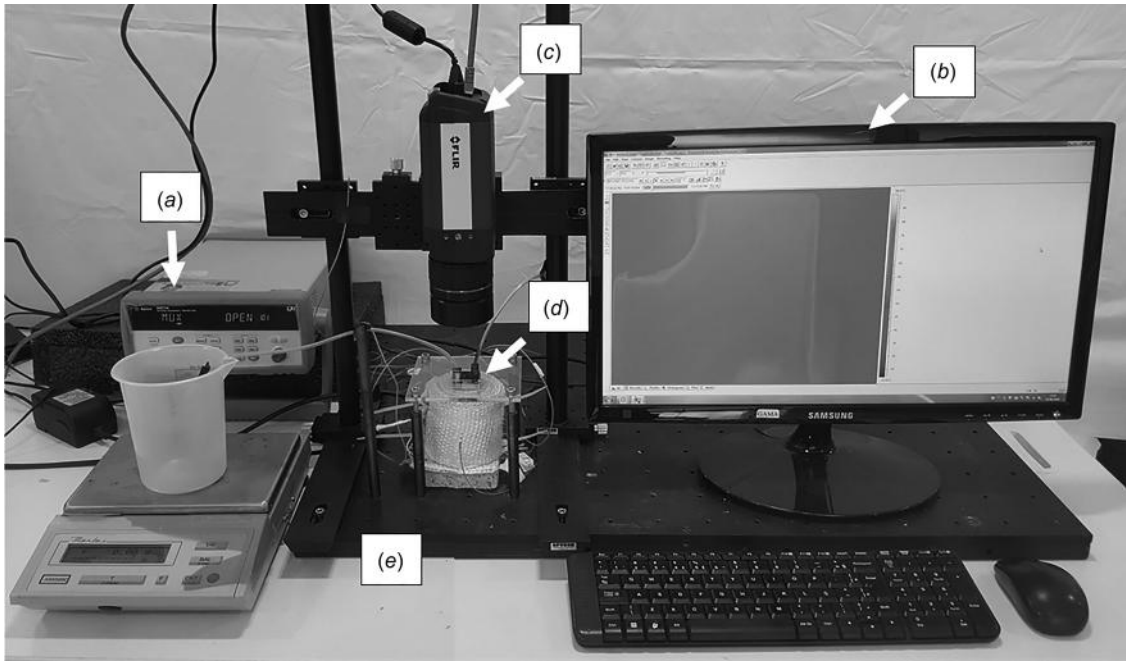

Fig. 8 Overview of the test bench: (*a*) data acquisition system, (*b*) computer for acquisition and data processing, (*c*) thermography camera, (*d*) heater system and (*e*) scale

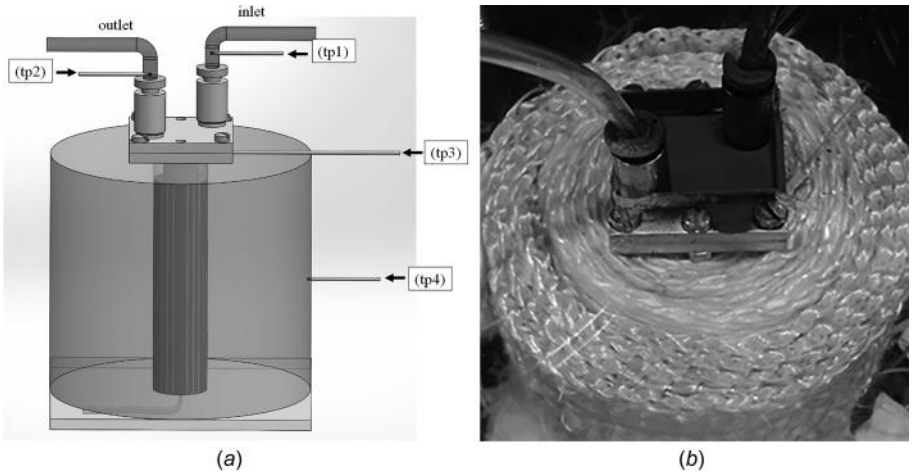

Fig. 9 Thermocouple positions: (tp1) inlet fluid port, (tp2) outlet fluid port, (tp3) contact between heating system and micro heat exchanger, and (tp4) fixed on the lateral external surface of insulation; (*a*) schematic drawing of the heat exchanger assembly and (*b*) assembled system

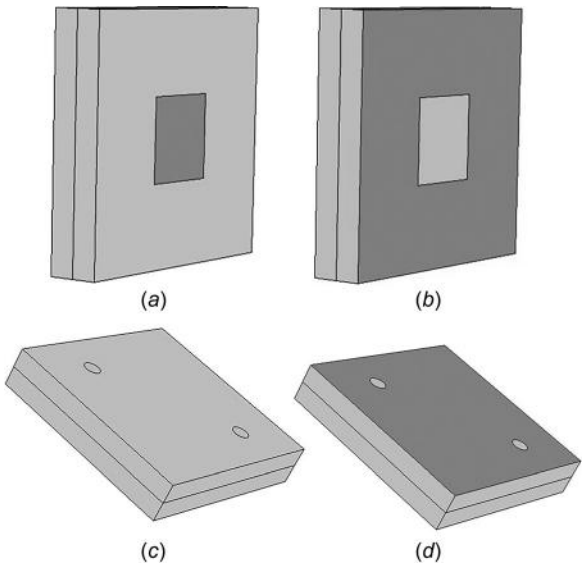

Fig. 10 Adopted boundary conditions in the computational simulation and their respective places of application illustrated by the dark grey region: (*a*) imposed heat flux (bottom face), (*b*) insulated area (bottom face), (*c*) natural convection and radiation heat losses (lateral faces), and (*d*) natural convection and radiation heat losses (top face)

for all the cases analyzed, and thus after this elapsed time, the thermal resistance is turned off.

Once all the temperature sensors have returned to room temperature, a new experimental run can be initiated. Data from these measurements are then imported to the MATHEMATICA software [36], and subsequent data handling involves built in functions on this platform for analysis and graphical representation. All experimental error bars presented are obtained from a repeatability analysis using at least five replicas.

3 Numerical Approach

A 3D numerical model of the heat exchanger was developed using the COMSOL MULTIPHYSICS 4.4 software [32], making use of the conjugated heat transfer equations with the following assumptions: internal flow, laminar regime, continuity conditions of heat flux and temperature at the solid–fluid interfaces, and constant thermophysical properties. The continuity, momentum, and energy equations were solved in order to model the fluid flow and heat transfer in the micro heat exchanger with the main boundary conditions as illustrated in Fig. 10. A uniform heat flux was imposed at the center of the bottom exchanger face, in a region of 100 mm^2 (Fig. 10(*a*)). The region immediately around it, at the bottom face and in contact with the fiberglass insulation, was considered to be insulated (Fig. 10(*b*)), while the lateral faces (Fig. 10(*c*)) and top face (Fig. 10(*d*)) walls were considered to be losing heat by both natural convection and radiation.

The input parameters considered in the analysis are taken from the experimental data and are presented in Table 2.

Before starting the numerical simulation of the micro heat exchanger itself in the COMSOL [32], a reduced mathematical model is proposed here to model the heating system comprising the heater, the cartridge, and the insulation cover, so as to reduce the overall modeling cost. This hybrid numerical–analytical treatment is based on reformulating the heat conduction problem for the heater cartridge through the so-called CIEA [27–31], which allow for the derivation of improved lumped-differential formulations. The idea is to reduce the model through integration in one or more space coordinates, employing Hermite formula for integration that take into account the boundary information in approximating the integrals [28]. The aim is to achieve a new formulation as simple as the classical lumped system analysis but with markedly improved accuracy, in light of the consideration of temperature gradients in the coordinates where the integration is performed.

In this sense, the transient heat conduction problem for the heating system was formulated, approximating the heater as a homogeneous cylinder with uniform volumetric heat generation rate, as presented in the energy equation for the temperature distribution below:

$$\frac{1}{\alpha}\frac{\partial T_{\text{cart}}(r,z,t)}{\partial t} = \frac{1}{r}\frac{\partial}{\partial r}\left(r\frac{\partial T_{\text{cart}}(r,z,t)}{\partial r}\right) + \frac{\partial^2 T_{\text{cart}}(r,z,t)}{\partial z^2} + \frac{G}{k_{\text{cart}}} 0 < \text{r} < \text{ri}, 0 < \text{z} < \text{H} \tag{1a}$$

where the heat source, G, can be related to the voltage applied to the heater and its volume by

$$G = \frac{V^2}{\text{Vol}*R} \tag{1b}$$

and considering the following boundary and initial conditions:

$$\left.\frac{\partial T_{\text{cart}}(r,z,t)}{\partial z}\right|_{z=0} = 0 \tag{1c}$$

$$T_{\text{cart}}(r,H,t) = T_c(t) \tag{1d}$$

$$\left.\frac{\partial T_{\text{cart}}(r,z,t)}{\partial r}\right|_{r=0} = 0 \tag{1e}$$

$$k_{\text{cart}}\left.\frac{\partial T_{\text{cart}}(r,z,t)}{\partial r}\right|_{r=r_i} + h_{\text{eff}}(T_{\text{cart}}(r_i,z,t) - T_\infty(t)) = 0 \tag{1f}$$

$$T_{\text{cart}}(r,z,0) = T_0 \tag{1g}$$

where the effective heat transfer coefficient can be described by Eq. (2), once the electrical–thermal analogy is applied to the thermal insulation, as

$$h_{\text{eff}} = \frac{1}{A_{\text{cart}}}\left(\frac{\ln\left(\frac{r_e}{r_i}\right)}{2\pi k_{\text{isol}}H} + \frac{1}{2\pi h_e r_e H}\right)^{-1} \tag{2}$$

From the definition of the heating element temperatures averaged across the r and z directions, we have

$$\bar{T}_{\text{cart}}(z,t) = \frac{1}{\pi r_i^2}\int_0^{r_i} 2\pi r T_{\text{cart}}(r,z,t)dr \tag{3a}$$

Table 2 Relevant data for the three experimental cases

Symbols (units)	Case 1	Case 2	Case 3
$\dot{m}$ (g/min)	20	24	28
T_∞ (°C)	25.97	26.61	25.83
T_{in} (°C)	35.74	37.05	36.34
h_{eff} (W/m^2 K)		3.08	
k_{isol} (W/m K)		4.3×10^{-2}	
k_{cart} (W/m K)		386	
A_{cart} (m^2)		3.4×10^{-3}	
V (V)		120	
R (Ω)		238	
P (W)		60.5	
Vol (m^3)		1.4×10^{-5}	
G (W/ m^3)		4.32×10^6	

$$\bar{\bar{T}}_{\text{cart}}(t) = \frac{1}{H}\int_0^H \bar{T}_{\text{cart}}(z,t)dz \tag{3b}$$

A lumped system analysis was then implemented in approximating the heat conduction problem in Eq. (1). It is assumed that in the radial direction, the traditional lumped analysis is sufficient to adequately approximate the averaged-temperature field along the radial coordinate, which essentially assumes the radially averaged value to equal the surface temperature value at $r = r_i$. On the other hand, an improved lumped-differential approach [27–31] is adopted in the axial direction, where more significant spatial variation in the temperature distribution is to be expected. Therefore, integrating Eq. (1*a*) first in the radial direction, then in the axial direction, making use of Eqs. (3*a*) and (3*b*) and the boundary and initial conditions given by Eqs. (1*c*)–(1*g*), problem (1) can be rewritten as

$$\frac{1}{\alpha}\frac{d\bar{\bar{T}}_{\text{cart}}(t)}{dt} = \frac{2h_{\text{eff}}}{r_i k_{\text{cart}}}\left(T_\infty(t) - \bar{\bar{T}}_{\text{cart}}(t)\right) + \frac{1}{H}\left[\left.\frac{\partial \bar{T}_{\text{cart}}(z,t)}{\partial z}\right|_{z=H} - \left.\frac{\partial \bar{T}_{\text{cart}}(z,t)}{\partial z}\right|_{z=0}\right] + \frac{G}{k_{\text{cart}}} \tag{4a}$$

and initial conditions are rewritten in terms of the average temperature

$$\bar{\bar{T}}_{\text{cart}}(0) = T_0 \tag{4b}$$

It is possible to achieve improved approximations for the average temperature using Hermite formulae for integrals [26], such as the $H_{1,1}$ and $H_{0,0}$ approximations, which are the corrected and trapezoidal rules, respectively, as presented in Eqs. (5a) and (5b) below:

$$H_{1,1} \rightarrow \int_0^h y(x)dx \cong \frac{h}{2}\left(y(0) + y(h)\right) + \frac{h^2}{12}\left(y'(0) - y'(h)\right) \tag{5a}$$

$$H_{0,0} \rightarrow \int_0^h y(x)dx \cong \frac{h}{2}\left(y(0) + y(h)\right) \tag{5b}$$

So, an improved approximation for the average temperature $\bar{\bar{T}}_{\text{cart}}(t)$, given in Eq. (3*b*), can be expressed using the formula $H_{1,1}$ from Eq. (5*a*), in the form

$$\bar{\bar{T}}_{\text{cart}}(t) = \frac{1}{H}\int_0^H \bar{T}_{\text{cart}}(z,t) \cong \frac{1}{H}\left\{\frac{H}{2}\left[\bar{T}_{\text{cart}}(0,t) + \bar{T}_{\text{cart}}(H,t)\right] - \frac{H^2}{12}\left[\left.\frac{\partial \bar{T}_{\text{cart}}}{\partial z}\right|_H - \left.\frac{\partial \bar{T}_{\text{cart}}}{\partial z}\right|_0\right]\right\} \tag{6a}$$

and the trapezoidal rule can be used to approximate the heat flux integral employing the $H_{0,0}$ formula, from Eq. (5*b*), as

$$\int_0^H \frac{\partial \bar{T}_{\text{cart}}}{\partial z}dz = \bar{T}_{\text{cart}}(H,t) - \bar{T}_{\text{cart}}(0,t) \cong \left[\frac{H}{2}\left.\frac{\partial \bar{T}_{\text{cart}}}{\partial z}\right|_H + \left.\frac{\partial \bar{T}_{\text{cart}}}{\partial z}\right|_0\right] \tag{6b}$$

An algebraic system with Eqs. (6a) and (6b), with the boundary conditions in the z direction, Eqs. (1*c*) and (1*d*), after averaging across the r direction, can be solved for the temperatures and temperature gradients at the boundaries, and then the following relations are determined:

$$\bar{T}_{\text{cart}}(0,t) = \frac{1}{2}\left(\bar{\bar{T}}_{\text{cart}}(t) - T_c(t)\right) \tag{7a}$$

$$\bar{T}_{\text{cart}}(H,t) = T_c(t) \tag{7b}$$

$$\left.\frac{\partial \bar{T}_{\text{cart}}}{\partial z}\right|_0 = 0 \tag{7c}$$

$$\left.\frac{\partial \bar{T}_{\text{cart}}}{\partial z}\right|_H = -\frac{3\left(\bar{\bar{T}}_{\text{cart}}(t) - T_c(t)\right)}{H} \tag{7d}$$

Such lumped-differential analysis is aimed at estimating the imposed heat flux to the heat exchanger substituting Eq. (7*d*) into the Fourier's Law applied at the bottom surface of the exchanger, $z = H$ (see Fig. 6)

$$q_z = -k_{\text{cart}}\left.\frac{d\bar{T}_{\text{cart}}(z)}{dz}\right|_{z=H} \tag{8}$$

However, the imposed heat flux will be a function of the average temperature $\bar{\bar{T}}_{\text{cart}}(t)$, which on the other hand is to be determined from the solution of the ordinary differential equation (4*a*). However, since the solution of interest here is for the steady-state regime only, one may neglect the transient term in Eq. (4*a*), and the mathematical formulation, with the use of Eq. (7*d*), can be rewritten as

$$0 = \frac{2h_{\text{eff}}}{r_i k_{\text{cart}}}\left(T_\infty - \bar{\bar{T}}_{\text{cart}}\right) - \frac{1}{H}\left\{\frac{3\left(\bar{\bar{T}}_{\text{cart}} - T_c\right)}{H}\right\} + \frac{G}{k_{\text{cart}}} \tag{9}$$

Equations (9) and (10) below need to be solved simultaneously within COMSOL MULTIPHYSICS [32], to appropriately represent the boundary condition in the dark grey region illustrated in Fig. 10(*a*), i.e.,

$$q_z = k_{\text{cart}}\left(\frac{3\left(\bar{\bar{T}}_{\text{cart}} - T_c\right)}{H}\right) \tag{10}$$

4 Results and Discussion

First, the experimental results for the three considered mass flow rates are presented, followed by the computer simulations making use of the experimental conditions reported herein, aimed at providing a critical comparison between the numerical and experimental analysis. In this sense, Fig. 11 illustrates the evolution of the temperature at the micro heat exchanger internal surface, in contact with the copper cartridge (measured by the thermocouple tp3), in dimensionless form, for five different runs of case 1 (mass flow rate of 20 g/min). The dimensionless temperature is defined as

$$\theta_c(t) = \frac{T_c(t) - T_c(0)}{T_\infty(t)} \tag{11}$$

The repeatability of the five experiments for case 1 (20 g/min) is clearly observable. A similar behavior was achieved for the other two mass flow rates. It can be noticed from Fig. 11 that within 60 min, the experiment has already reached steady-state. At steady-state, the average temperature for mass flow rate of 20 g/min was 161.8 °C with a standard deviation of 1.3 °C; for mass flow rate of 24 g/min, it was 158.3 °C with a standard deviation of 0.7 °C; and for 28 g/min, it was 154.2 °C with a standard deviation of 0.9 °C. As expected, the interface temperature gradually decreases with the increase of the mass flow rate.

Figure 12 shows the evolution of the difference between the outlet and inlet water bulk temperatures, as obtained from the thermocouples tp2 and tp1with the error bars estimated from the repeatability analysis with five replicas. Figure 13 presents the inlet (three bottom curves) and the outlet (three top curves) bulk temperatures after 40 min of experiment. As expected, the outlet fluid temperature decreases with the increase on mass flow rate. At steady-state, the inlet fluid bulk temperature for the mass flow

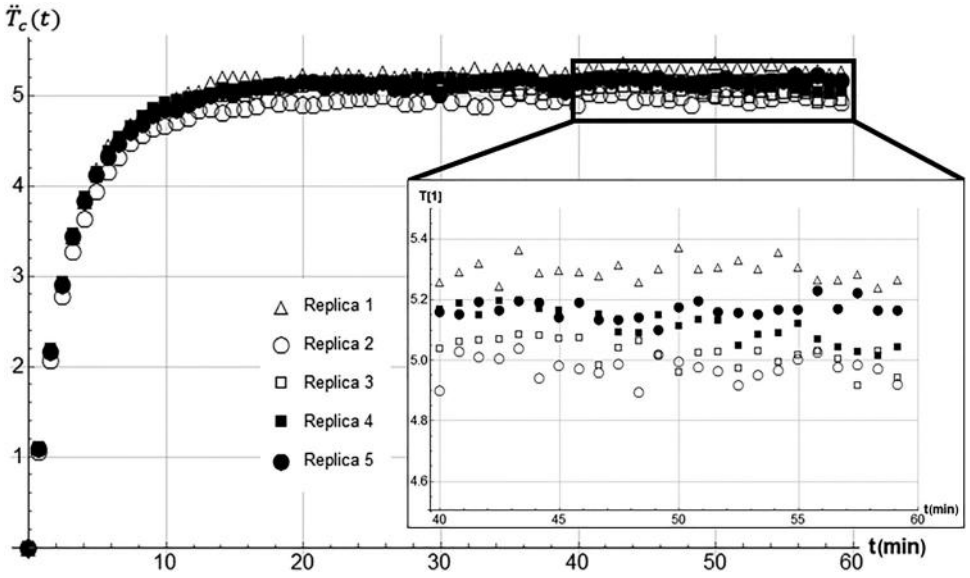

Fig. 11 Dimensionless temperature at the micro heat exchanger lower surface, at the contact with the copper cartridge, for five repeated tests at the flow rate of 20 g/min (case 1)

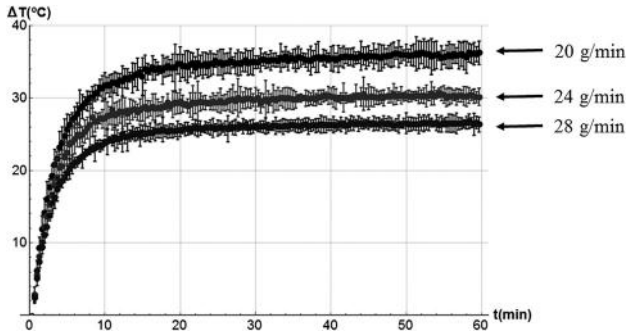

Fig. 12 Difference between the outlet (tp2) and inlet (tp1) water temperatures obtained from the thermocouple measurements, i.e., $\Delta T = tp2 - tp1$

rate of 20 g/min was estimated as 35.4 °C with a standard deviation of 0.3 °C, while for 24 g/min it was 36.6 °C with standard deviation of 0.5 °C, and for 28 g/min it was 35.8 °C with standard deviation of 0.6 °C. On the other hand, the outlet fluid bulk temperature for the mass flow rate of 20 g/min was 71.3 °C with a standard deviation of 0.2 °C; for 24 g/min, it was 67.0 °C with

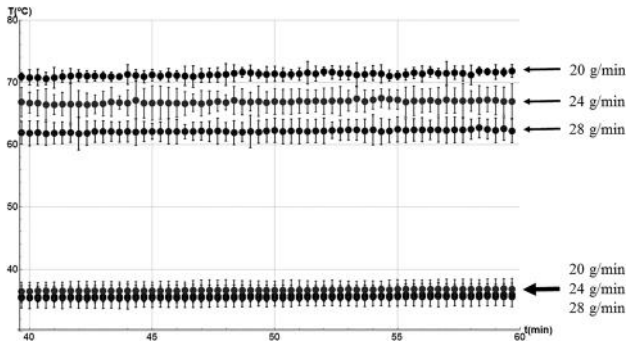

Fig. 13 Outlet (three top curves) and inlet (three bottom curves) water temperatures obtained from the thermocouples measurements, tp2 and tp1, respectively, after 40 min and up to steady-state

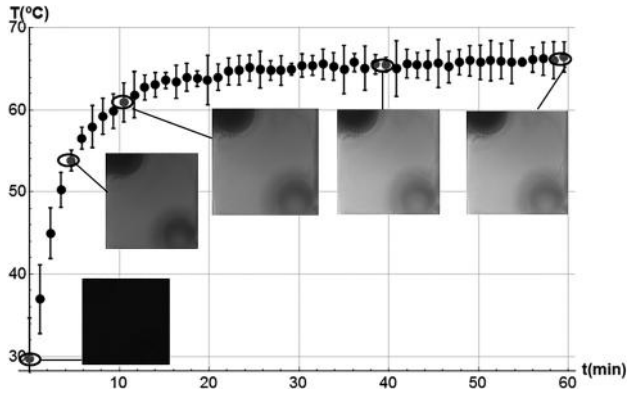

Fig. 14 Evolution of average surface temperature (dots) of the top external surface for case 1 and the corresponding infrared images for five different times

standard deviation of 0.6 °C; and for 28 g/min, it was 62.4 °C with standard deviation of 0.7 °C.

Figure 14 shows the evolution of the top surface temperature, as obtained from infrared thermography, and averaged on a 13 mm × 13.2 mm area on the external surface of the micro heat exchanger, corresponding to the microchannels total area just below the top cover. Also shown are the corresponding infrared images for five different instants, associated with the dots that represent the average temperatures over this 13 mm × 13.2 mm area.

Table 2 summarizes some important experimental data, for the three cases analyzed here, that will be used as input for the

Table 3 Mesh refinement runs for the grid independence analysis

Total number of elements (Nξ)	Maximum element size, ξ (mm)
383,472	0.496
2,648,633	0.174
4,896,429	0.15
5,491,042	0.14
6,328,931	0.13
7,332,547	0.12

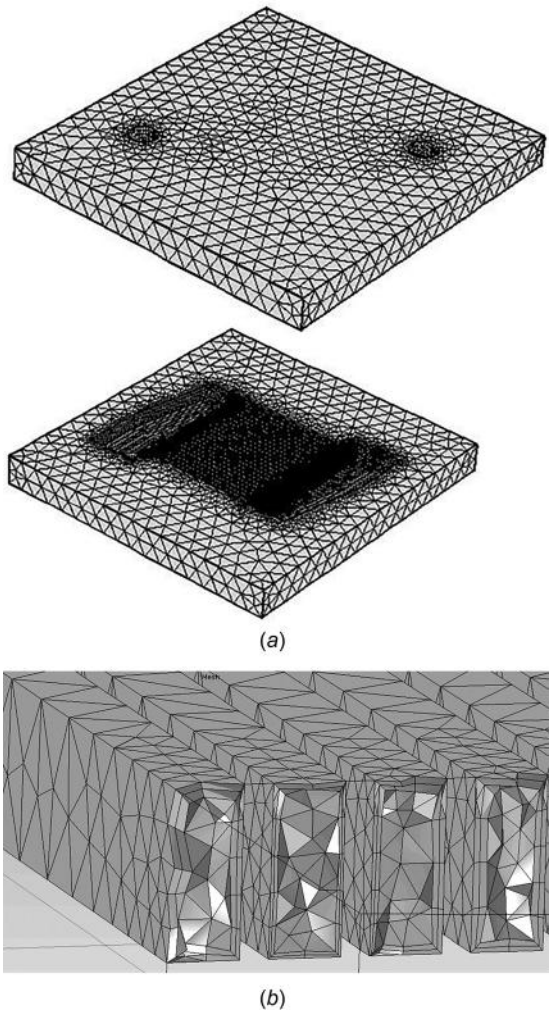

Fig. 15 Illustration of the computational grid for the case with a total of 383,472 elements: (*a*) Mesh for the base and cover of the micro heat exchanger and (*b*) mesh at microchannels region

theoretical analysis. For the fluid (water) and for the heat exchanger walls material (aluminum), was used the library of properties of COMSOL, for temperature-dependent thermophysical properties.

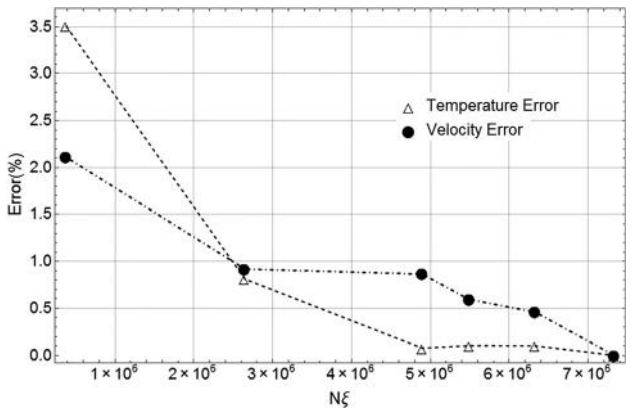

Fig. 16 Error reduction in both average velocity and top surface temperature with the increase on the total number of elements (Nξ) in the computational grid

For the present conduction–convection–radiation numerical simulation, first of all, a grid independence analysis was carried out using data from case 1, in terms of the maximum element size (ξ) and the total number of elements (Nξ). In this sense, the maximum element size was varied, mainly in the fluid region, thereby varying the total number of elements in the mesh. As a result, the computational time jumped from 40 min for the case with 383,472 elements in the grid, to almost 36 h for the case with 7,332,547 elements in the grid, on an Intel Xeon 2.10 GHz, with 128 GB RAM. Table 3 presents the number of elements (Nξ) and the maximum element size (ξ) for each analyzed grid.

Figure 15(*a*) shows the computational grid for the base and the cover of the micro heat exchanger, while Fig. 15(*b*) shows the grid in transverse view at the microchannels region, both for the case with a total of 383,472 elements. Figure 16 shows the reduction on computational error with the increase on the total number of elements (Nξ), corresponding to the relative error of the average velocity in a cross section located in the middle of the microchannel length and to the relative error of the average temperature on the top surface of the micro heat exchanger. This relative error was estimated based on the most refined mesh, and clearly indicates that it is monotonically reducing when the number of elements in the mesh increases, as expected. In the following analysis and in the comparisons against the experimental data, the simulation results obtained with the most refined mesh (7,332,547 elements in the grid) were used throughout as best estimates.

Figure 17 presents a comparison of the fluid bulk temperatures at the outlet of the micro heat exchanger for the three cases, from 40 min up to steady-state. The solid lines represent the numerical simulation results for the steady-state, and the symbols are for the experimental results, reaching steady-state by the end of the experiment. This comparison shows the reasonably good agreement between the predictions and the test data, within the experimental error bars.

The infrared thermography measurements were also compared with the simulated temperature data for the external surface temperature on the top surface of the micro heat exchanger. Figure 18 presents a typical infrared image with two central lines that transversely (red line) and longitudinally (green line) cross the external top surface of the micro heat exchanger, along with some theoretical–experimental measurements will be presented below.

Figure 19 shows the comparison of the external top surface temperatures, at steady-state, for the numerical (in color) and experimental (in black) estimates, with mass flow rate of 20 g/min over the area corresponding to the microchannels region (i.e., the black square region in Fig. 18). The experimental surface temperature, averaged over this black square region, is 67.0 °C with a standard deviation of 0.3 °C, while the same averaged surface temperature from the numerical simulation yields 67.4 °C. Although not graphically presented here, a similar analysis was performed for the mass flow rate of 24–28 g/min. For a mass flow

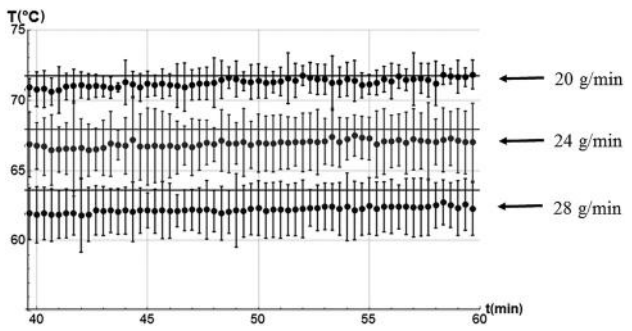

Fig. 17 Comparison between steady-state numerical (solid line) results and experimental results (dots) from $t = 40$ min up to steady-state, of the outlet fluid bulk temperature, for the three cases analyzed

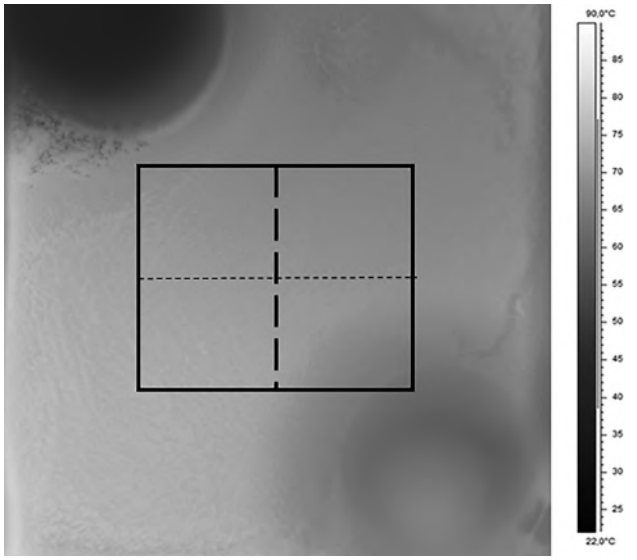

Fig. 18 Typical infrared thermographic image with two central lines that transversally (dashed line) and longitudinally (dotted line) cross the external top surface of the micro heat exchanger

rate of 24 g/min, the experimental averaged surface temperature is 63.6 °C with a standard deviation of 0.2 °C, while the simulated result is 64.5 °C. For a mass flow rate of 28 g/min, the experimental average surface temperature is 60.5 °C with a standard deviation of 0.3 °C, while the simulated average surface temperature is 60.7 °C.

Figure 20 shows the comparison between the numerical (solid line) and the experimental results (symbols) of the external top surface temperature along the longitudinal (green line illustrated in Fig. 18) and transversal (red line in Fig. 18) centerlines of the microchannels region, at steady-state, for mass flow rate of 28 g/min). Again, a good agreement is achieved, with a deviation of at most 2.5 °C.

Table 4 consolidates the major comparative results from the experimental and theoretical thermal analyses of the designed micro heat exchanger, for the three different mass flow rates. From the measured and simulated outlet temperatures, the total heat transfer rate to the fluid (Q) can be determined, yielding relative deviations of at most 2.4% in case of mass flow rate of 24 g/min (case 2).

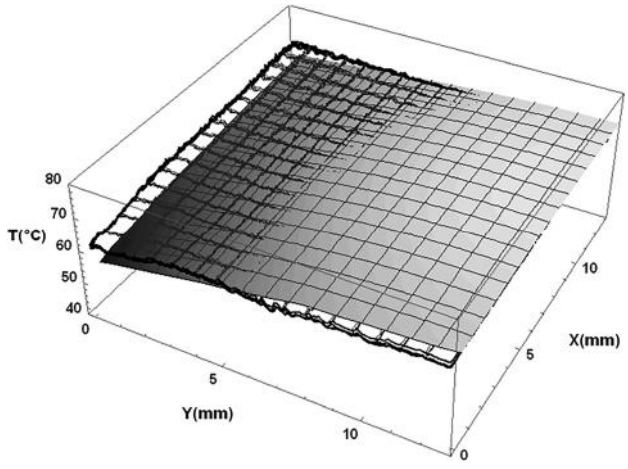

Fig. 19 Experimental (hollow contour) and numerical results (solid contour) for the temperatures at the external top surface of the micro heat exchanger for a mass flow rate of 20 g/min

The most important parameter that can be determined from the experimental analysis of this microthermal system is the global heat transfer coefficient, U. According to heat exchangers theory, it is given as

$$U = \frac{Q}{A.\mathrm{LMTD}} \tag{11a}$$

where the log mean temperature difference is given by

$$\mathrm{LMTD} = \frac{(T_{\mathrm{out}} - T_{\mathrm{in}})}{\mathrm{Log}\left(\frac{T_c - T_{\mathrm{in}}}{T_c - T_{\mathrm{out}}}\right)} \tag{11b}$$

The obtained global heat transfer coefficient can be directly compared to a theoretically proposed correlation for fully developed Nusselt numbers in rectangular microchannels, for prescribed heat flux boundary conditions (H2 condition) [37], valid for $0.1 \leq a \leq 10$ and laminar flow condition. Here, the case of one single heated wall is considered, corresponding to the exchanger bottom wall in contact with the resistance. The recommended correlation is then given by

$$\begin{aligned} \mathrm{Nu}_{H2} = {} & 1.6980 \times 10^{-4} a^6 - 5.7050 \times 10^{-3} a^5 \\ & + 7.5552 \times 10^{-2} a^4 - 0.5054 a^3 \\ & + 1.8448 a^2 - 3.8559 a + 5.2720 \end{aligned} \tag{12}$$

where a is the aspect ratio of the rectangular microchannel, in this case equal to 0.423.

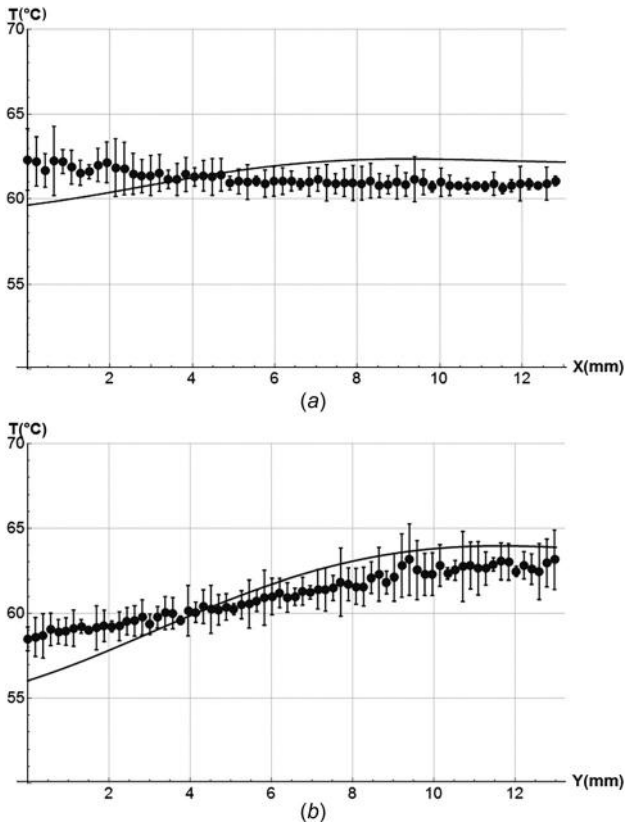

Fig. 20 Comparison of surface temperatures along longitudinal and transversal centerlines: numerical (solid line) and experimental (dots) temperatures at the external top surface of the micro heat exchanger (mass flow rate of 28 g/min): (*a*) longitudinal centerline and (*b*) transversal centerline

Table 4 Consolidation of experimental and simulation results

	Symbol (units)	Exp.	Num.	Exp.	Num.	Exp.	Num.
Mass flow rate	$\dot{m}$ (g/min)	20		24		28	
Room temperature	T_∞ (°C)	25.97		26.61		25.83	
Average top surface temperature	T_w (°C)	67.05	67.40	63.59	64.54	60.49	60.74
Inlet fluid temperature	T_{in} (°C)	35.74		37.05		36.34	
Outlet fluid temperature	T_{out} (°C)	71.21	71.39	67.20	67.92	63.19	63.60
Thermal load in the fluid	Q (W)	49.43	49.69	50.42	51.62	52.37	53.17
Heat losses	Q_L (%)	17.27	16.35	15.76	13.32	12.60	10.84

Table 5 Comparison of experimental and theoretically correlated [37] global heat transfer coefficients, U (W/m^2 ° C)

Mass flow rate (g/min)	20	24	28
U corr. (W/m^2 °C) (Eq. 11*b*) [37]	4395.83	4395.83	4395.83
U exp. (W/m^2 °C)	4593.78	4771.07	5004.78

The global heat transfer coefficient is determined from Eq. (11) and based on the experimental data presented in Table 4, as well as from the correlation in Eq. (12), to yield the results in Table 5. The correlation here employed for comparison is based on numerical simulations for the case of one single wall being uniformly heated, while the other three walls are kept insulated. Although these simplified conditions are not exactly the same as for the real situation dealt with here, such a comparison allows for the inspection of the deviations that might occur when the thermal experimental setup does not perfectly match the available working expressions. Clearly, there is an increasing deviation between the present experimental values for the global heat transfer coefficient with respect to the values obtained from the theoretical correlation for idealized conditions. Certainly, at such microscale device, effects such as conjugated heat transfer and axial heat diffusion, play some role in the thermal behavior, requiring more detailed modeling to recover the present experimental results, such as demonstrated by the excellent agreement of the experimental and simulation results presented in Table 4. Therefore, correlations based on over simplified theoretical models and/or experimental results for macroscale devices should be employed with care for micro heat exchangers.

5 Conclusion

A micro heat exchanger was designed to cool a multijunction photovoltaic cell employed in a HCPV system and recover the resulting waste heat. Prior to its installation and testing in the actual HCPV module, a theoretical–experimental study was carried out in order to understand the thermal behavior of the proposed micro heat exchanger. Experimental runs were performed for three different mass flow rates, so as to analyze the effect on the micro heat exchanger internal surface temperature and on the temperature difference between the inlet and outlet fluid ports. Regarding the theoretical analysis, a hybrid numerical–analytical simulation was implemented aiming at computational cost reduction, combining the analytical solution of a lumped-differential heat conduction model for the heater cartridge, with a finite elements numerical solution for the micro heat exchanger, where the adopted boundary conditions were as close as possible to the actual experimental situation. The improved lumped-differential formulation was derived for the heater-cartridge system analysis, through the CIEA, then coupled to the finite element method solution (COMSOL) of the conjugated heat transfer problem in the microdevice.

Good agreement between the experimental and numerical results was demonstrated, with regard to fluid and wall temperatures. In addition, an existing correlation for the global heat transfer coefficient in fully developed flow and prescribed uniform heat flux conditions has been employed to offer a critical comparison with the experimentally determined values. Such analysis showed that microscale effects not accounted for in the simplified model, such as the conjugated heat transfer and fin effects promoted by the heat exchanger external and internal walls, can limit the range of applicability of the simpler practical correlations and require more advanced computational analysis for further design improvement.

Acknowledgment

The authors would like to acknowledge the financial support provided by the Brazilian agencies (CNPq and FAPERJ). CPNC would like to acknowledge the hospitality of the Mechanical Engineering Department of the University College London, UK, during the final preparation of the manuscript.

Funding Data

- Conselho Nacional de Desenvolvimento Cientifico e Tecnologico (BOLSA DE PRODUTIVIDADE and Edital UNIVERSAL MCTI).
- Fundacao Carlos Chagas Filho de Amparo a Pesquisa do Estado do Rio de Janeiro (E_06/2015—Jovem C and Edital FAPERJ No 41).

Nomenclature

a = aspect ratio of the rectangular microchannel
A_{cart} = lateral area of the cooper cartridge (m^2)
A_s = surface area (m^2)
c_p = specific heat (kJ/kg K)
g = gravity acceleration (m/s^2)
G = volumetric heat generation rate (W/ m^3)
Gr_L = local Grashof Number
h = hermite integration interval
H = height of the copper cartridge (m)
h_{av} = average convection heat transfer coefficient (W/m^2 K)
h_e = external convective heat transfer coefficient (W/m^2 K)
h_{eff} = effective heat transfer coefficient (W/m^2 K)
$H_{0,0}$ = trapezoidal integration rule
$H_{1,1}$ = corrected trapezoidal integration rule
HCPV = high concentration photovoltaic system
k_{air} = thermal conductivity of air (W/m K)
k_{cart} = thermal conductivity of the resistance cartridge (W/m K)
k_{isol} = thermal conductivity of the thermal insulation (W/m K)
L_c = characteristic length (m)
LMTD = log mean temperature difference
$\dot{m}$ = mass flow rate (g/min)
Nu_{av} = average dimensionless Nusselt number
Nu_{H2} = Nusselt numbers correlation for prescribed heat flux boundary conditions
$N\xi$ = number of elements in the grid
P = dissipated power in the electrical resistance (W)
Pr = dimensionless Prandtl number
Q = thermal load in the fluid (W)

q_z = heat flux component in the z direction (W/m^2)
Q_{air} = heat losses by natural convection (W)
Q_L = system losses (%)
Q_{rad} = heat losses by radiation (W)
R = electrical resistance (Ω)
r_e = outer radius of the thermal insulation (m)
r_i = inner radius of the thermal insulation (m)
r, z = spatial coordinates
t = time (s)
T = temperature (°C)
T_c = contact temperature at the micro heat exchanger and the copper cartridge interface (°C)
T_{cart} = local heating system temperature (°C)
T_f = film temperature (°C)
T_{in} = fluid temperature at the inlet of the micro heat exchanger (°C)
T_{out} = fluid temperature at the outlet of the micro heat exchanger (°C)
T_w = surface temperature (°C)
T_∞ = external ambient temperature (°C)
T_0 = initial temperature (°C)
$\bar{T}_{cart}$ = averaged cross section heating system temperature (°C)
$\bar{\bar{T}}_{cart}$ = volume-averaged heating system temperature (°C)
tp = thermocouple
u = velocity (m/s)
U = overall heat transfer coefficient (W/°C m^2)
V = voltage (V)
Vol = volume of the copper cartridge (m^3)
x, y = spatial coordinates
θ_c = dimensionless contact temperature at the micro heat exchanger and the copper cartridge interface

Greek Symbols

α = thermal diffusivity (m^2/s)
β = coefficient of thermal expansion (K^{-1})
ΔT = temperature difference (°C)
ν_{air} = air kinematic viscosity (Pa·s)
ξ = maximum element size in the grid (mm)
σ = Stephan–Boltzmann constant (W/(m^2 K^4))
$\in$ = emissivity of the micro heat exchanger surface [1]

References

[1] Guerrieri, D. C., and Naveira-Cotta, C. P., 2014, "Experimental and Theoretical Analysis of a Microchannel Heat Exchanger for High Concentration Photovoltaic Cells," ICCHMT International Symposium on Convective Heat and Mass Transfer (CONV-14), Kusadasi, Turkey, June 8–13, pp. 1–12.
[2] Correa, M., Guerrieri, C. D., Naveira-Cotta, C. P., and Colman, J., 2013, "Design and Manufacture of Microchannel Heat Sinks for High Concentration Photovoltaic Cells," 22th International Congress of Mechanical Engineering (COBEM), Ribeirão Preto, SP, Brazil, Nov. 3–7, pp. 1–12.
[3] Ohadi, M. M., Choo, K., Dessiatoun, S. V., and Cetegen, E., 2012, *Next Generation Microchannel Heat Exchangers*, Springer, New York.
[4] Ameel, T. A., Warrington, R. O., Wegeng, R. S., and Drost, M. K., 1997, "Miniaturization Technologies Applied to Energy Systems," Energy Convers. Manage.,**38**(10–13), pp. 969–982.
[5] Khan, M. G., and Fartaj, A., 2011, "A Review on Microchannel Heat Exchangers and Potential Applications," Int. J. Energy Res., **35**(7), pp. 553–582.
[6] Escher, W., Brunschwiler, T., Michel, B., and Poulikakos, D., 2010, "Experimental Investigation of an Ultrathin Manifold Microchannel Heat Sink for Liquid-Cooled Chips," ASME J. Heat Transfer., **132**(8), p. 081402.
[7] Arie, M. A., Shooshtari, A. H., Dessiatoun, S. V., Al-Hajri, E., and Ohadi, M. M., 2015, "Numerical Modeling and Thermal Optimization of a Single-Phase Flow Manifold-Microchannel Plate Heat Exchanger," Int. J. Heat Mass Transfer, **81**, pp. 478–489.
[8] Knupp, D. C., Naveira-Cotta, C. P., Renfer, A., Tiwari, M. K., Cotta, R. M., and Poulikakos, D., 2015, "Analysis of Conjugated Heat Transfer in Micro-Heat Exchangers Via Integral Transforms and Non-Intrusive Optical Techniques," Int. J. Numer. Methods Heat Fluid Flow, **25**(6), pp. 1444–1462.
[9] Zimmermann, S., Helmers, H., Manish, T. K., Paredes, S., Michel, B., Wiesenfarth, M., Bett, A. W., and Poulikakos, D., 2015, "A High-Efficiency Hybrid High-Concentration Photovoltaic System," Int. J. Heat Mass Transfer, **89**, pp. 514–521.
[10] Rahimi, M., Asadi, M., Karami, N., and Karimi, E., 2015, "A Comparative Study on Using Single and Multi Header Microchannels in a Hybrid PV Cell Cooling," Energy Convers. Manage., **101**, pp. 1–8.
[11] Besheer, A. H., Smyth, M., Zacharopoulos, A., Mondol, J., and Pugsley, A., 2016, "Review on Recent Approaches for Hybrid PV/T Solar Technology," Int. J. Energy Res., **40**(15), pp. 2038–2053.
[12] Radwana, A., Ookawara, S., and Ahmed, M., 2016, "Analysis and Simulation of Concentrating Photovoltaic Systems With a Microchannel Heat Sink," Sol. Energy, **136**, pp. 35–48.
[13] Xu, Z., and Kleinstreuer, C., 2014, "Computational Analysis of Nanofluid Cooling of High Concentration Photovoltaic Cells," ASME J. Therm. Sci. Eng. Appl., **6**(3), p. 031009.
[14] Micheli, L., Sarmah, N., Luo, X., Reddy, K. S., and Mallick, T. K., 2013, "Opportunities and Challenges in Micro-and Nano-Technologies for Concentrating Photovoltaic Cooling: A Review," Renewable Sustainable Energy Rev., **20**, pp. 595–610.
[15] Phelan, P., Otanicar, T., Taylor, R., and Tyagi, H., 2013, "Trends and Opportunities in Direct-Absorption Solar Thermal Collectors," ASME J. Therm. Sci. Eng. Appl., **5**(2), p. 021003.
[16] Costa Junior, J. M., Naveira-Cotta, C. P., Nunes, J., and Tostado, C. P., 2015, "Design, Fabrication and Characterization of Micro-Reactor for Biodiesel Synthesis," Heat Pipe Sci. Technol., **6**(3–4), pp. 135–153.
[17] Pontes, P. C., Chen, K., Naveira-Cotta, C. P., Costa Junior, J. M., Tostado, C. P., and Quaresma, J. N. N., 2016, "Mass Transfer Simulation of BiodieselSynthesis in Microreactors," Comput. Chem. Eng. J., **93**, pp. 36–51.
[18] Pontes, P. C., Naveira-Cotta, C. P., and Quaresma, J. N. N., 2017, "Three-Dimensional Reaction-Convection-Diffusion Analysis With Temperature Influence for Biodiesel Synthesis in Micro-Reactors," Int. J. Therm. Sci., **118**, pp. 104–122.
[19] Little, A. B., and Garimella, S., 2012, "Waste Heat Recovery in Data Centers Using Sorption Systems," ASME J. Therm. Sci. Eng. Appl., **4**(2), p. 021007.
[20] Herold, K. E., and Radermacher, R., 2002, "Integrated Power and Cooling Systems for Data Centers," Eighth Intersociety Conference on Thermal and Thermomechanical Phenomena in Electronic Systems (ITHERM), San Diego, CA, May 30–June 1, pp. 808–811.
[21] Morini, G. L., 2004, "Single-Phase Convective Heat Transfer in Micro-Channels: A Review of Experimental Results," Int. J. Therm. Sci., **43**(7), pp. 631–651.
[22] Maranzana, G., Perry, I., and Maillet, D., 2004, "Mini and Micro-Channels: Influence of Axial Conduction in the Walls," Int. J. Heat Mass Transfer., **47**(17–18), pp. 3993–4004.
[23] Hetsroni, G., Mosyak, A., Pogrebnyak, E., and Yarin, L. P., 2005, "Heat Transfer in Microchannels: Comparison of Experiments With Theory and Numerical Results," Int. J. Heat Mass Transfer, **48**(25–26), pp. 5580–5601.
[24] Nunes, J. S., Cotta, R. M., Avelino, M., and Kakaç, S., 2010, "Conjugated Heat Transfer in Micro-Channels," *Microfluidics Based Microsystems: Fundamentals and Applications* (NATO Science for Peace and Security Series A: Chemistry and Biology, Vol. 1), S. Kakaç, B. Kosoy, and Pramuanjaroenkij, eds., Springer, New York, pp. 61–82.
[25] Knupp, D. C., Naveira-Cotta, C. P., and Cotta, R. M., 2014, "Theoretical-Experimental Analysis of Conjugated Heat Transfer Nanocomposite Heat Spreaders with Multiple Micro-Channels," Int. J. Heat Mass Transfer, **74**, pp. 306–318.
[26] Cotta, R. M., Knupp, D. C., and Naveira-Cotta, C. P., 2016, *Analytical Heat and Fluid Flow in Microchannels and Microsystems* (Mechanical Eng. Series), Springer-Verlag, New York.
[27] Aparecido, J. B., and Cotta, R. M., 1989, "Improved One-Dimensional Fin Solutions," Heat Transfer Eng., **11**(1), pp. 49–59.
[28] Cotta, R. M., and Mikhailov, M. D., 1997, *Heat Conduction: Lumped Analysis, Integral Transforms, Symbolic Computation*, Wiley, New York.
[29] Alves, L. S. B., Sphaier, L. A., and Cotta, R. M., 2000, "Error Analysis of Mixed Lumped-Differential Formulations in Diffusion Problems," Hybrid Methods Eng., **2**(4), pp. 409–435.
[30] Naveira-Cotta, C. P., Lachi, M., Rebay, M., and Cotta, R. M., 2010, "Experiments and Simulations in Transient Conjugated Conduction-Convection-Radiation," Heat Transfer Res., **43**(3), pp. 209–231.
[31] Knupp, D. C., Naveira-Cotta, C. P., Ayres, J. V. C., Cotta, R. M., and Orlande, H. R. B., 2012, "Theoretical-Experimental Analysis of Heat Transfer in Nonhomogeneous Solids Via Improved Lumped Formulation, Integral Transforms and Infrared Thermography", Int. J. Therm. Sci., **62**, pp. 71–84.
[32] COMSOL Multiphysics, 2015, "COMSOL Multiphysics User's Guide," Version 4.4, COMSOL Multiphysics: Modeling, Finite Element Analysis and Engineering Simulation Software.
[33] Chávez Toro, C. A., 2014, "Heat Transfer and Pressure Drop of Hydro- Carbon Refrigerants During Flow Boiling in a Microchannel Array," Ph.D. thesis, University of São Paulo, São Carlos, SP, Brazil.
[34] Siva, V. M., Pattamatta, A., and Das, S. K., 2013, "A Numerical Study of Flow and Temperature Maldistribution in a Parallel Microchannel System for Heat Removal in Microelectronic Devices," ASME J. Therm. Sci. Eng. Appl., **5**(4), p. 041008.
[35] Commenge, J. M., Falk, L., Corriou, J. P., and Matlosz, M., 2002, "Optimial Design for Flow Uniformity in Microchannel Reactors," AIChE J., **48**(2), pp. 345–358.
[36] Wolfram, S., 2015, *The Mathematica Book*, Wolfram Media, Cambridge, UK.
[37] Dharaiya, V. V., and Kandlikar, S. G., 2012, "Numerical Investigation of Heat Transfer in Rectangular Microchannels Under H2 Boundary Condition During Developing and Fully Developed Laminar Flow," ASME J. Heat Transfer., **134**(2), p. 0209111.